

Quantitative TEM analysis of a hexagonal mesoporous silicate structure

S. Hudson,^{ac} D. A. Tanner,^{*ab} W. Redington,^a E. Magner,^{ac} K. Hodnett^{ac} and S. Nakahara^{ad}

Received 24th April 2006, Accepted 12th June 2006

First published as an Advance Article on the web 21st June 2006

DOI: 10.1039/b605581h

TEM analysis of mesoporous materials is generally undertaken to give qualitative results. Accurate quantitative analysis is demonstrated in this study. A systematic image analysis of a powder form of a hexagonal mesoporous material known as KIT-6 is conducted using a transmission electron microscope (TEM). Three types of image contrast typically appear in this material (a hexagonal honeycomb structure, wide and narrow parallel lines). The honeycomb face is used to characterise this material in terms of a conventional 2-D hexagonal structure and the *d*-spacings for the (100) and (110) planes are experimentally measured in varying focus conditions. A tilting experiment is conducted to determine how the angle of tilt affects the line spacing and their visibility. Tilting has very little effect on the line spacing, whereas it affects the visibility of both the wide and narrow lines by limiting an angle range of visibility. The hexagonal lattice structure parameter determined by TEM method is found to be ~7% lower than that calculated by low-angle X-ray diffraction. Thus we conclude that TEM data can be used to determine the geometry and dimensions of hexagonal mesoporous silica materials, with a small error in the hexagonal lattice parameter.

Introduction

A family of ordered mesoporous silicates, M41S, was first developed by Mobil researchers in 1992.¹ This new family of materials consisted of self-assembled mesoporous materials containing a unique architecture of ordered pore structure with a narrow pore size distribution. They were formed *via* a co-operative assembly route, whereby the inorganic moiety, *e.g.* amorphous silica is condensed between ordered surfactant micelles. The discovery of M41S attracted considerable interest in mesoporous materials for possible applications in the area of catalysis and sensors.^{1,2} Other families of mesoporous materials include folded sheet materials, FSM-16,³ SBA-x,⁴ and hexagonally-packed mesoporous transition metal molecular sieves⁵ to mention only a few. Research groups have demonstrated the possibility of precisely controlling the structure of the final products by varying reactants and reaction conditions, for example, the surfactant,⁶ the source of silica,³ co-solvents,⁶ pH,⁷ and temperature.⁸

A number of transmission electron microscope (TEM) studies on the powder form of mesoporous materials have been published in recent years. While the TEM images give a clear indication of ordered structure with long narrow channels and ordered pore openings, in many cases a clear explanation of what is actually being observed has not been presented.^{4,5,9} These images are often misinterpreted primarily

due to a lack of understanding of the TEM image contrast. When Beck *et al.*¹⁰ first reported these new mesoporous materials, they provided a brief description of how the bright-field (BF) images of their materials were recorded under various focus conditions. They noted how “images show contrast reversal upon going through Gaussian focus” and concluded that the mesoporous silicates could be described as a “weak phase object”. More recent work,^{11,12} on the other hand, does not seem to distinguish between phase and amplitude contrast clearly, referring repeatedly to “diffraction contrast”. Thus it appears appropriate to understand the contrast mechanism of the BF images taken by conventional TEM, so that the observed image contrast can be interpreted correctly for practical use.

Prompted by a need to understand the contrast mechanism of the BF images, a conventional TEM analysis of mesoporous materials was undertaken using the hexagonally ordered material KIT-6. The amplitude contrast is negligibly small in these materials and a majority of the BF image contrast arises from the phase contrast induced by defocusing. The validity of taking measurements from the defocused TEM images to estimate the dimensions of the pore structure was analysed by varying the tilt angle and focus depth, and the TEM data were compared with those obtained by the X-ray diffraction method.

Experimental procedure

A hexagonal KIT-6 mesoporous material was synthesised according to the methods described by Kleitz and co-workers.^{13,14} In a typical synthesis, 6 g of Pluronic P123 surfactant (BASF) was dissolved in a solution containing 217 g of distilled water and 11.8 g of HCl (35%, Sigma), followed by

^a Materials & Surface Science Institute, University of Limerick, Limerick, Ireland

^b Department of Manufacturing and Operations Engineering, University of Limerick, Limerick, Ireland. E-mail: David.Tanner@ul.ie; Tel: +353-61-234130

^c Department of Chemical and Environmental Sciences, University of Limerick, Limerick, Ireland

^d Department of Physics, University of Limerick, Limerick, Ireland

the addition of 6 g of butanol (99%, Sigma) under stirring at 35 °C. After 1 h, 12.9 g of TEOS (tetraethoxysilane) (Sigma) was added and the reaction mixture was left stirring at 35 °C for 24 h. The reaction mixture was then heated in an autoclave under static conditions for 24 h at 100 °C. The surfactant was removed by Soxhlet extraction with ethanol (Sigma).

Low-angle X-ray powder diffraction patterns were recorded on a Philips X'Pert MPD PRO X-ray diffractometer (PW 3050/60) using Cu K α radiation ($\lambda = 0.154$ nm) run at 40 kV and 35 mA. The instrument has an automatic divergent slit resulting in an irradiated length of 10 mm. The step size used was 0.0167° at 15 s step⁻¹ in the low-angle range of $0.3 \leq 2\theta \leq 10^\circ$.

To obtain the porosity of mesoporous materials, a Micromeritics ASAP 2010 system was used to measure nitrogen gas adsorption/desorption isotherms at 77 K. The samples were degassed by heating under vacuum at 393 K for 12 h. The pore size data were analysed by the thermodynamics-based Barrett–Joyner–Halenda (BJH) method¹⁵ on the desorption branch of the N₂ isotherm.

A TEM specimen was prepared by first mixing the mesoporous silicate powder in ethanol and then by placing the drop onto a Formbar-backed carbon-coated copper grid. Transmission electron microscopy was conducted using a JEOL JEM-2011 electron microscope operated at an accelerating voltage of 200 kV. Images were recorded with a Gatan DualVision 600™ CCD camera attached to the microscope and were analysed using Gatan Digital Micrograph Version 3.6.5.

Results and discussion

X-ray diffraction and porosimetry

A low-angle X-ray diffraction pattern from the KIT-6 material is presented in Fig. 1, which shows three prominent peaks corresponding to the 100, 110, and 200 reflections within the 2θ angle range of 0–5°. The appearance of these peaks is consistent with that given by Kresge *et al.*¹ Since the use of

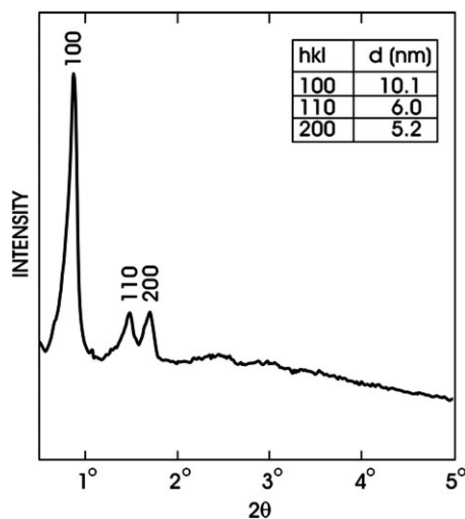


Fig. 1 A low angle powder X-ray diffraction pattern from KIT-6, which shows three prominent peaks of 100, 110, and 200.

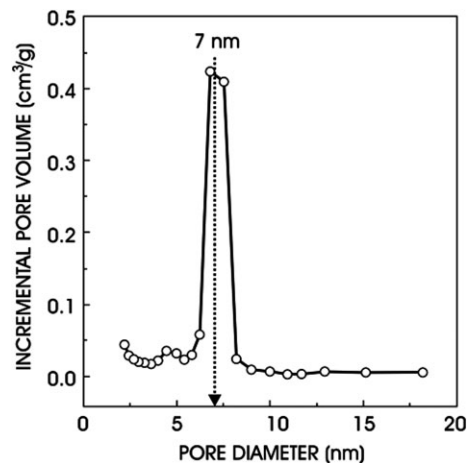


Fig. 2 A nitrogen porosimetry plot, indicating that a KIT-6 mesoporous material contains pores whose average pore size is 7 nm.

three indices in a hexagonal symmetry system can be a little confusing, we will elaborate the indexing scheme in a later section of this paper. Nevertheless, the appearance of sharp peaks indicates that this amorphous silica is well ordered, forming a hexagonal lattice.

While an X-ray diffraction method provides information about the structure of silica material, porosimetry can give the size distribution of pores in this material. The incremental pore volume is plotted against the pore size in Fig. 2. A narrow peak is located around the pore size of 7.0 nm from BJH theory. There has been some controversy over the optimum theory for calculating pore diameters or to characterise mesoporous materials with porous walls. Recent publications have indicated that BJH theory may underestimate pore size by as much as 20%.¹⁶

Image contrast by TEM

The major contrast source in amorphous materials such as silica is amplitude contrast that originates from mass-thickness variations.¹⁷ In the case of mesoporous silica materials, the presence of pores changes the effective thickness along the electron-beam direction of the TEM, thus producing amplitude contrast associated with thickness variations. An additional contrast source, which is phase contrast, can be introduced by defocussing. This defocusing effect is demonstrated in Fig. 3. Fig. 3 is a series of micrographs taken in (a) overfocus ($\Delta f = +2.0$ μm), (b) in-focus ($\Delta f = \sim 0$ μm), and (c) underfocus ($\Delta f = -2.0$ μm) conditions. The symbol, Δf , is the amount and sign of defocus. An identical area is enclosed with a white square. It is noted that the image taken under an in-focus condition is vanishingly weak, suggesting that a thickness variation within this porous material is not large enough to produce strong amplitude contrast. In defocused conditions, on the other hand, high-contrast images appear in both over- and under-focus conditions (see Fig. 3a and c). These defocused images are phase contrast introduced by defocusing. The thickness variation in this material introduces a significant phase shift to an incident beam, which interferes at a defocused plane and finally forms Fresnel fringes around the

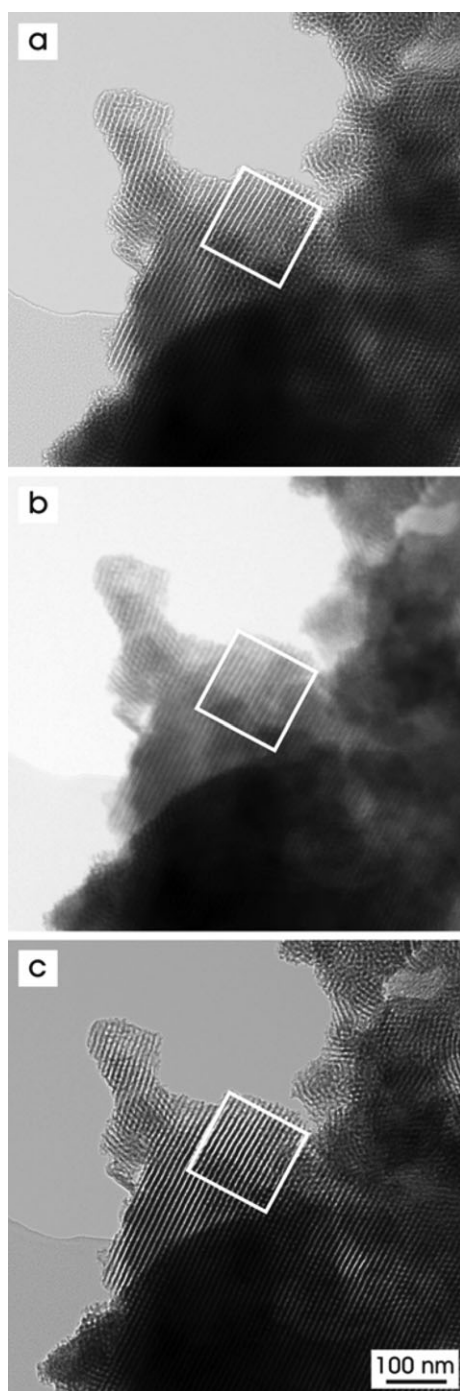


Fig. 3 TEM micrographs showing the effect of focussing on variations in the image contrast of W-type lines in a KIT-6 mesoporous material. The images were taken under (a) overfocus ($\Delta f = +2.0 \mu\text{m}$), (b) in-focus ($\Delta f = \sim 0 \mu\text{m}$), and (c) underfocus ($\Delta f = -2.0 \mu\text{m}$) conditions. The symbol, Δf , denotes the amount and sign of defocus. The same area is indicated with a white square box.

structural feature. The images shown in Fig. 3 clearly demonstrate that the phase contrast enhances the structural details and thus is a dominant contrast mechanism in this material. In this sense, KIT-6 is a phase object.

It should be mentioned that most of published images are unintentionally taken in underfocus conditions, because

underfocussed images not only bring out the sharpest contrast, but also provide material density fluctuations correctly; a high-density region appears darker than a low-density area. Thus our eyes tend to image an object in the underfocus condition. In the following discussion, we will present TEM images taken in underfocussed conditions unless otherwise specified.

Geometry of mesoporous silica particles

TEM provides various morphological aspects of the KIT-6 mesoporous material. With the TEM, we found three characteristic features present abundantly in this material, as seen in Fig. 4. These features include (a) a honeycomb structure, (b) parallel lines with wide spacing, and (c) parallel lines with narrow spacing (see white square boxes in Fig. 4). These image features can be understood from the geometry of a single particle. In the case of the hexagonal KIT-6, the particle can be described roughly as an elongated ellipsoid. Fig. 5 is a schematic view showing the hexagonally-ordered structure of a single mesoporous particle. Here the structure of a hexagonally-ordered material is drawn in an idealised fashion but it is expected that the real structure will be more distorted. We found that most of the particles lie along the length of the honeycomb tubes on the specimen plane. The reason for the frequent appearance of this configuration is that this position is most stable due to its lower centre of gravity. Since many particles from the powder sample appear to lay flat on the specimen plane, the images of the ordered honeycomb face were not observed as frequently as the parallel lines.

From the particle geometry in Fig. 5, it can be ascertained that there are primarily three high symmetry directions as indicated with symbols, H, W, and N. If the particle is imaged along these three directions, it will exhibit the images corresponding to those shown in Fig. 4. It is clear that the H projection gives a honeycomb structure, whereas the W and N projections yield widely- and narrowly-spaced parallel lines. Fig. 6 further illustrates how such wide and narrow parallel lines are formed along the W and N projections. Here we have established the origin of three characteristic image features from purely geometrical considerations.

Crystallography of mesoporous silica material

Based on the above experimental observations, we can now define a 2-D hexagonal coordinate for the mesoporous particle consistent with X-ray and TEM diffraction results. Some caution has to be exercised for indexing a hexagonal cell. For a hexagonal unit cell, a 4-indices system known as Miller–Bravais lattice is generally used. For example, the Miller–Bravais indices of a plane are denoted by $h, k, i,$ and l enclosed in parentheses, (hki) . In this system, the third index is the negative of the addition of the first and the second indices; $h + k = -i$. Accordingly, for a conventional method of using Miller indices, it is customary to adopt a 3-indices system by omitting the third index, which yields $(hk \cdot l)$. The period at the third position is generally omitted. Keeping this simplification in mind, we shall use the Miller indices in the subsequent discussion.

We define an expanded hexagonal unit cell by two vectors, a_1 and a_2 in Fig. 7a and b. This choice of the hexagonal cell is

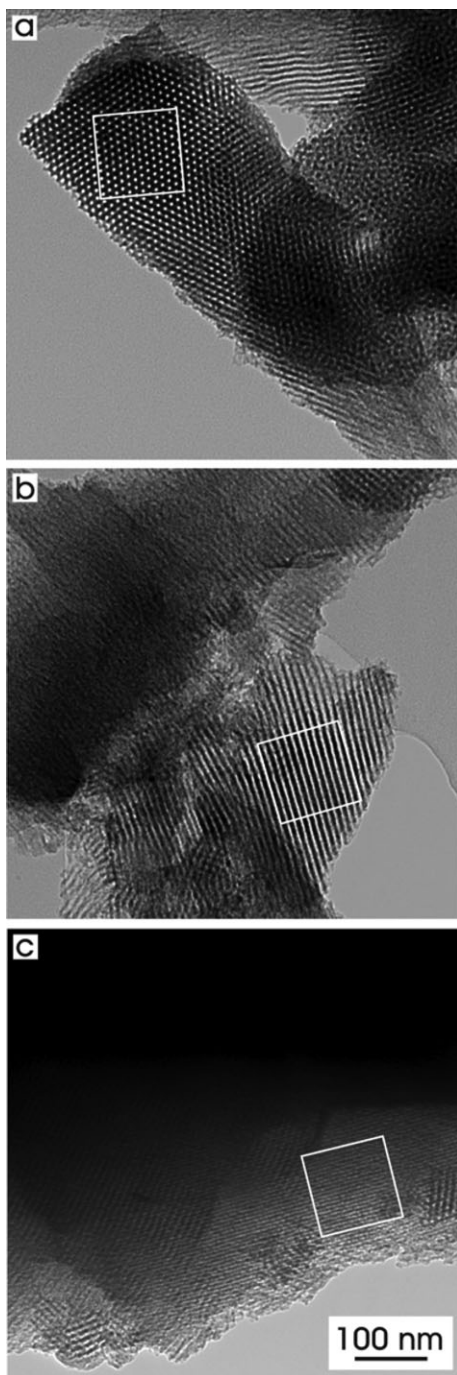


Fig. 4 Three typical TEM images taken from a hexagonal KIT-6 mesoporous material, showing (a) a honeycomb structure, (b) wide parallel lines, and (c) narrow parallel lines.

consistent with the indexed peaks in the X-ray spectrum shown in Fig. 1 as well as that given by Kresge *et al.*¹ An expanded view of (a) is further illustrated in Fig. 7b, in which a lattice constant, a , three planes, (100), (010), (110), and their respective interplanar spacings (d_{100} , d_{010} , d_{110}) are shown. In this hexagonal lattice, the lattice constant, a , is the distance from pore centre to pore centre. Electron or X-ray diffraction occurs on these planes and form respective diffraction spots perpen-

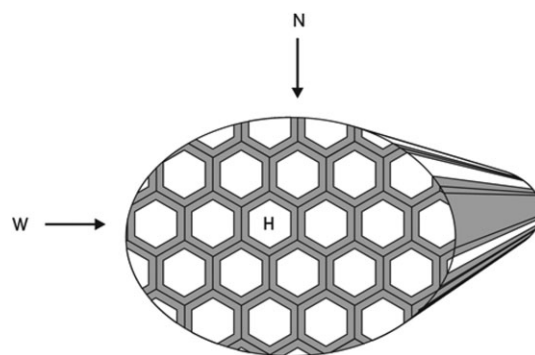


Fig. 5 Geometry of a single mesoporous particle, which can be examined from three symmetry directions, H, W, and N, are indicated.

dicular to the planes in a reciprocal space. Accordingly, the corresponding reciprocal lattice defined by a_1^* and a_2^* together with diffraction spots is drawn in Fig. 7c. A low-angle electron diffraction pattern from a hexagonal KIT-6 mesoporous material is shown in Fig. 8a. The indexed pattern is given in Fig. 8b. A similar pattern was obtained in MCM-41 by Kresge *et al.*¹ Four rings, which pass through the major diffraction spots, 100, 110, 200, and 120, are also drawn in Fig. 8b. An X-ray powder diffraction pattern often contains these four reflections as diffraction peaks.¹

From the hexagonal coordinate defined in Fig. 7, it is possible to determine the line spacing for the W and N projections, d_W and d_N . The following relationships can be obtained;

$$d_W = d_{100} = \sqrt{3}a/2 \quad (1)$$

$$d_N = d_{110} = a/2 \quad (2)$$

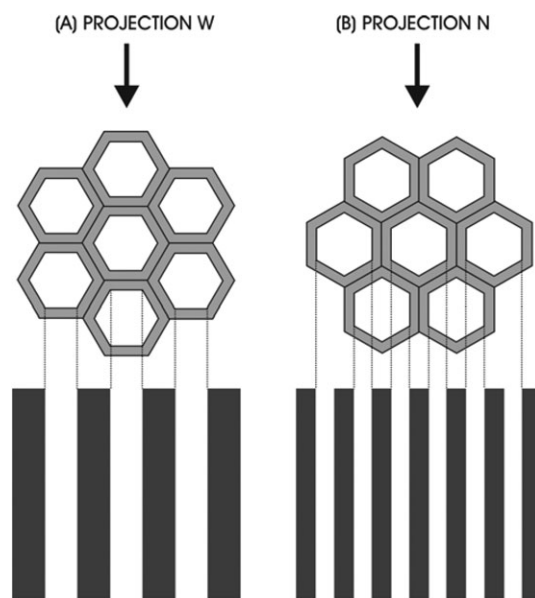


Fig. 6 Projections along two symmetry orientations, (A) W and (B) N, which yield the images wide and narrow parallel lines in a hexagonal KIT mesoporous material.

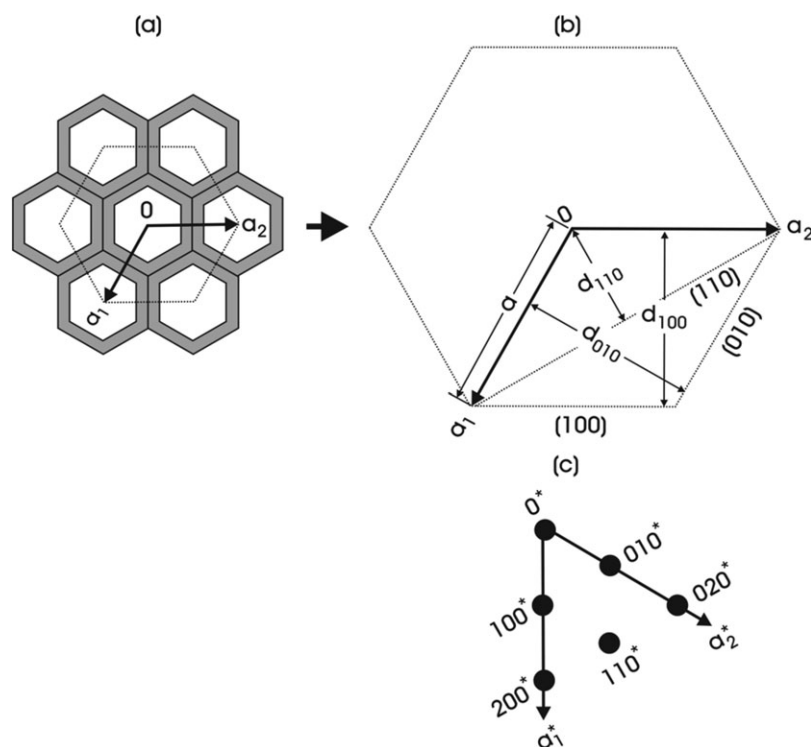


Fig. 7 Two-dimensional hexagonal coordinate defining the crystallography of a mesoporous particle. (a) A hexagonal unit cell defined by two vectors, a_1 and a_2 . (b) An expanded view of (a) that contain a lattice constant, a , three planes ((100), (010), (110)), and their respective interplanar spacings (d_{100} , d_{010} , d_{110}). (c) The corresponding reciprocal lattice, which is defined by a_1^* and a_2^* , and diffraction spots (100^* , 010^* , 110^*).

Formulae (1) and (2) can be used to determine d_{100} , d_{110} and a from d_W and d_N . The size of the mesopore opening cannot be directly measured by TEM measurements in the W or N projections or by XRD analysis. Such analyses will give the d -spacing between planes in a hexagonal structure, as shown in Fig. 6. To the best of our knowledge, this is the first direct measurement of the d_{110} plane spacing from TEM images of mesoporous materials. Measurements of the pore openings taken from images along the H projection may vary to a large extent with the orientation of the particle and thus values taken this way should be compared carefully to values obtained from nitrogen adsorption/desorption analysis. Comparing the pore opening and the d -spacing values can give an indication of wall thickness of the structure, Table 1. The hexagonal unit cell parameter, a , is $\sim 7\%$ lower when measured using TEM analysis compared to XRD analysis. The value of a obtained by XRD is a bulk measurement while the TEM value is an average of a minimum of 30 particles measured.

Effect of focussing on the spacing of W and N parallel lines

The values of d_W and d_N were plotted as a function of the amount and sign of defocus (see Fig. 9). For this study, a peak-to-peak distance for the bright lines was taken as the value of d_W and d_N (measurements for the dark lines indicated that the distances were equivalent). The line profile tool in Digital Micrograph allowed us to measure the average of at least 10 lines. Both d_W and d_N values slowly decrease with increasing amount of underfocus. The amount of the decrease appears to

be larger for d_W than for d_N . A reason for the decreasing trend seen in Fig. 9 is not immediately clear at the moment, but as long as the defocus amount is chosen to be small ($\sim -2 \mu\text{m}$), the values of d_W and d_N should be close to the real geometrical value. A theoretical contrast calculation will be made to evaluate this trend in the future.

Effect of specimen tilting on the visibility and the spacings of W and N parallel lines

It has been shown, here and in the literature,¹² that the appearance of the W- and N-type lines depends on the orientation of the particle with respect to the electron-beam direction. As is clear from Fig. 6, if the particle is rotated by $\pm 30^\circ$ along the long axis, the W projection should switch to the N projection and *vice versa*. We conducted a tilting experiment while measuring the change in the values of d_W and d_N . In this experiment, images were recorded at tilting increments of 2° . Fig. 10 demonstrates how the W-type lines (enclosed inside a white square) become visible or invisible, depending on the angle of tilt. The parallel lines lie along the tilt axis, which is indicated with a symbol, TA. Fig. 10a and b were taken at tilt angles of 2° and 18° , respectively.

The d -spacing and visibility of W- and N-type parallel lines is plotted as a function of tilt angle in Fig. 11. Here the superscripts, T and X, imply d -spacing values obtained by TEM and X-ray diffraction, respectively. It is noted that the average angle between the appearance of the W- and N-type lines is $\sim 30^\circ$ as predicted. Both lines are visible within a limited range of tilt angle. The angle range of visibility is $\sim 12^\circ$

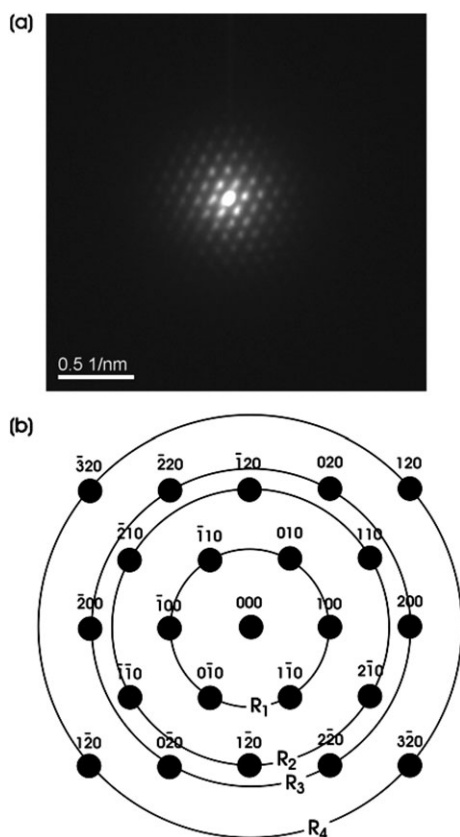


Fig. 8 A low-angle electron diffraction pattern from a hexagonal KIT mesoporous material, showing (a) experimental and (b) indexed patterns. Four rings, which are often observed in a low-angle X-ray diffraction pattern, are inserted in (b).

for the W-type lines, whereas it is $\sim 4^\circ$ for the N-type. As an invisible region is approached, the definition of the W- and N-type lines diminishes and a roughness in the images is observed. The small window of visibility for the N-type lines further supports an experiment that the N-type lines are not frequently observed. The d values change very little within the visible angle range, suggesting that the d values can be measured without considering the orientation as long as the images are visible. The d_{100}^T and d_{110}^T values are less than the corresponding X-ray values. Considering the fact that TEM measures a single particle and X-ray takes the average of many particles, the correspondence is quite reasonable.

The d value with the tilt angle of θ will change by a factor of $\cos \theta$, which will be $\cos \theta \approx 0.98$ for the maximum tilt angle of 12° . Thus the maximum tilting of 12° contributes to about 2%

Table 1 Comparison of d -spacings, unit cell parameters and wall thickness of KIT-6 calculated by XRD and TEM analyses, respectively

	d_{100}/nm	d_{110}/nm	a/nm	Wall thickness ^a /nm
XRD	10.1	6.0	11.8	4.8
TEM	9.7	5.4	11.0	4.0

^a Wall thickness = $a - D_{\text{BJH}}$.

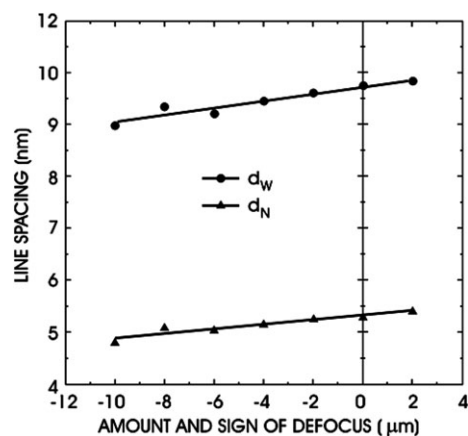


Fig. 9 Line spacings, d_W and d_N , for the wide and narrow lines measured from TEM images as a function of the amount and sign of defocus.

change in the d value. Within the visible angle range, the d_{100}^T value varies from 9.0 to 9.4 nm, which corresponds to about a 4% change, which is larger than that introduced by tilting. Therefore, the tilt effect on the d value can be ignored.

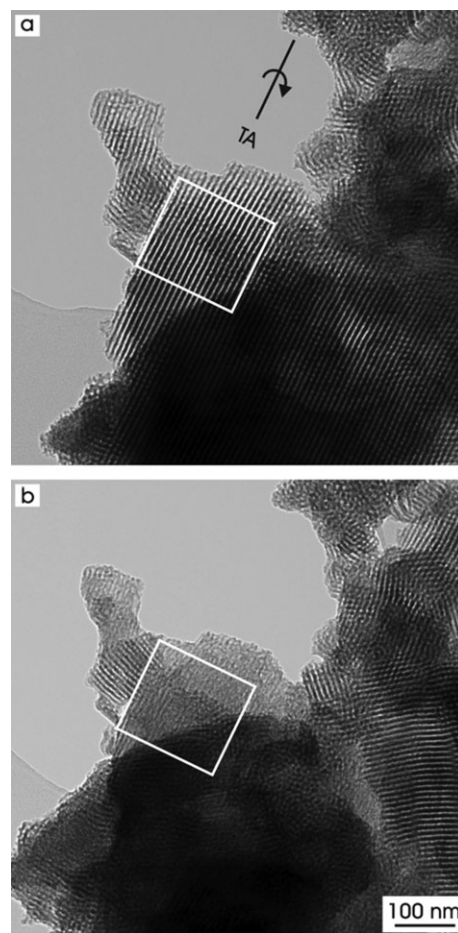


Fig. 10 Two (a) visible and (b) invisible images (a white square) of the W-type parallel lines taken at tilt angles of 2 and 18° . The tilt axis is indicated with a symbol, TA.

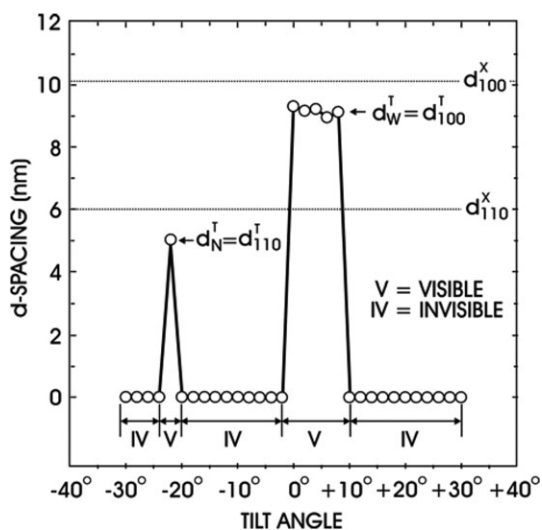


Fig. 11 Effect of specimen tilting on the d -spacing and visibility of W- and N-type parallel lines.

Finally, the visibility angle range can be estimated using a simple geometrical consideration. Details for the estimate are described in Appendix A. Based on this geometrical analysis, we plotted theoretical curves of specimen thickness vs. tilt angle for $D = 3.5$ and 7.0 nm, which correspond to the widths of the low-density region in the W- and N-type lines, respectively (see Fig. 12). These curves can give an estimate of the maximum allowable angle for line visibility. In a 100 nm thick specimen, the angle range of visibility is about 4 and 8° for W- and N-type lines. Considering the nature of a rough estimate, these angle values appear to be in good agreement with experimental 4 and 12° . This example further supports the fact that a geometrical analysis is sufficient to interpret TEM results for mesoporous materials.

Conclusion

TEM phase contrast (defocus) technique can be used to accurately determine the geometry of a hexagonal mesoporous

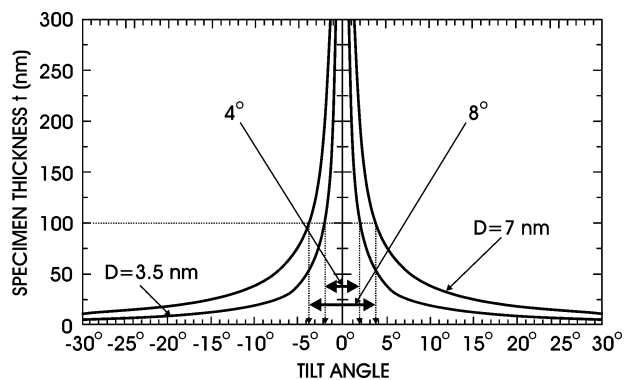


Fig. 12 Theoretical curves of specimen thickness vs. tilt angle, $\theta = \tan^{-1}(\frac{D}{t})$, which provides an estimate of the maximum allowable angle for line visibility. The curves are plotted for two pore sizes, $D = 3.5$ and 7.0 nm. For a 100 nm thick specimen, the maximum allowable angles for W- and N-type lines are 4 and 8° , respectively.

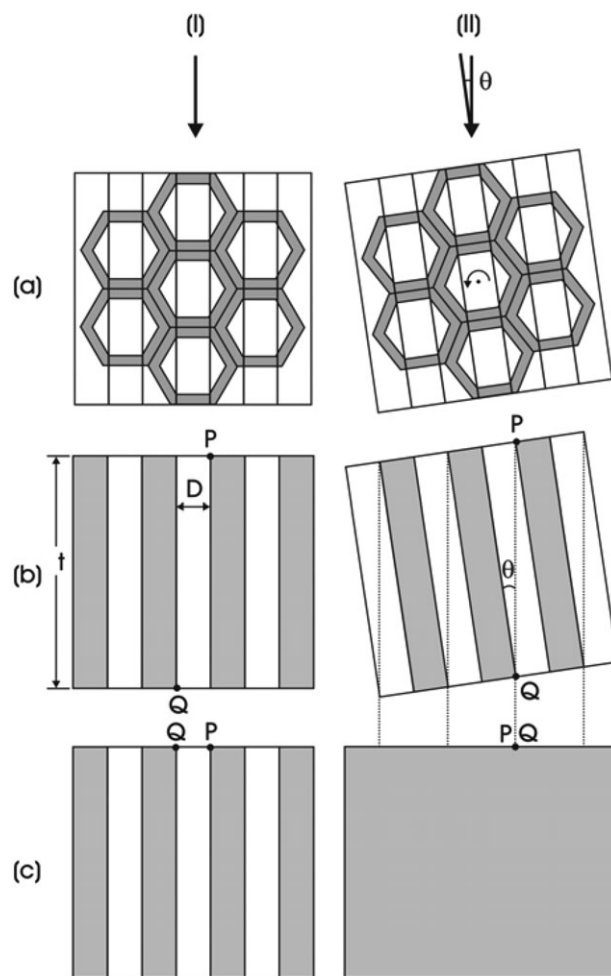


Fig. 13 A schematic diagram showing how the visibility angle range of W-type parallel lines can be estimated by dividing high- and low-density regions, which produce dark and bright images. A tilt angle, at which the neighbouring high-density regions overlap, defines the maximum allowable angle for line visibility.

material, KIT-6. Three characteristic image contrast features were observed, which are hexagonal honeycomb structure, wide and narrow parallel lines. The distance between the wide and narrow parallel lines was found to correspond to the d_{100} and d_{110} plane spacings, respectively. Care should be taken when interpreting images where the edge definition of the lines has deteriorated. This is the first report of experimental measurements of the d_{110} spacing from TEM images. The honeycomb structure was used to define the structure of this material in terms of a conventional hexagonal lattice. A specimen tilting experiment was conducted to observe how the angle of tilt affects the line spacing and visibility. Very little effect was found on the line spacing, whereas the visible images of the wide and narrow lines appear only in a limited angle range. Measurements of pore sizes from images taken in the H direction (the honeycomb structure) are inconsistent due to different orientations of the particle face. The lattice constant determined by TEM method is lower than that determined by low-angle X-ray diffraction by

approximately 7%. It can be determined from the images without knowing their orientation.

Appendix A

A tilting experiment in Fig. 11 has demonstrated that there is a maximum allowable angle of tilt before the line images become invisible. Here we illustrate a simple geometrical method for estimating such an angle for both the W- and N-type lines. Using the illustration given in Fig. 4, we show the method in Fig. 13. Along the W direction, we divide the mesoporous material into high- and low-density regions, which are effectively projected as dark and bright lines on the image plane. The simplified high-/low-density blocks are shown in (b). A specimen tilting involves the collective rotation of these blocks as shown in (ii). It is easy to see that if a tilt angle reaches a critical angle when the points P and Q overlap in the image plane, the line images become invisible. This angle, θ , can be determined from a simple geometrical relationship;

$$\theta = \tan^{-1}\left(\frac{D}{t}\right) \quad (\text{A1})$$

where D is the width of the low-density region and t is the specimen thickness. Using the relationship (A1), we plotted the specimen thickness vs. the tilt angle in Fig. 12. The average value of D was taken from Fig. 4. The case of the W and N projections corresponds to 7.0 and 3.5 nm, respectively. Again, care should be taken when interpreting images where the edge definition of the lines has diminished.

Acknowledgements

Financial support of this work by Enterprise Ireland, Science Foundation Ireland (ETS Walton fellowship to S.N.) and the Higher Education Authority of Ireland through the

Programme for Research in Third Level Institutions (1999–2000) is gratefully acknowledged.

References

- 1 C. T. Kresge, M. E. Leonowicz, W. J. Roth, J. C. Vartuli and J. S. Beck, *Nature*, 1992, **359**, 710.
- 2 Y. Lu, R. Ganguli, C. A. Drewien, M. T. Anderson, C. J. Brinker, W. I. Gong, Y. X. Guo, H. Soyez, B. Dunn, M. H. Huang and J. I. Zink, *Nature*, 1997, **389**, 364.
- 3 S. Inagaki, A. Koiwai, N. Suzuki, Y. Fukushima and K. Kuroda, *Bull. Chem. Soc. Jpn.*, 1996, **69**, 1449.
- 4 D. Y. Zhao, Q. Huo, J. Feng, B. F. Chmelka and G. D. Stucky, *J. Am. Chem. Soc.*, 1998, **120**, 6024.
- 5 D. M. Antonelli, A. Nakahira and J. Y. Ying, *Inorg. Chem.*, 1996, **35**, 3126.
- 6 D. Zhao, J. Sun, Q. Li and G. D. Stucky, *Chem. Mater.*, 2000, **12**, 275.
- 7 X. Y. Bao, X. S. Zhao, S. Z. Qiao and S. K. Bhatia, *J. Phys. Chem. B*, 2004, **108**, 16441.
- 8 J. Fan, C. Yu, J. Lei, Q. Zhang, T. Li, B. Tu, W. Zhou and D. Zhao, *J. Am. Chem. Soc.*, 2005, **127**, 10794.
- 9 Q. S. Huo, R. Leon, P. M. Petroff and G. D. Stucky, *Science*, 1995, **268**, 1324.
- 10 J. S. Beck, J. C. Vartuli, W. J. Roth, M. E. Leonowicz, C. T. Kresge, K. D. Schmitt, C. T.-W. Chu, D. H. Olson, E. W. Sheppard, S. B. McCullen, J. B. Higgins and J. L. Schlenker, *J. Am. Chem. Soc.*, 1992, **114**, 10834.
- 11 K. P. de Jong, A. H. Janssen, P. van der Voort and A. J. Koster, *Stud. Surf. Sci. Catal.*, 2003, **146**, 271.
- 12 A. H. Janssen, C.-M. Yang, Y. Wang, F. Schuth, A. J. Koster and K. P. de Jong, *J. Phys. Chem. B*, 2003, **107**, 10552.
- 13 F. Kleitz, S. H. Choi and R. Ryoo, *Chem. Commun.*, 2003, 2136.
- 14 T. W. Kim, F. Kleitz, B. Paul and R. Ryoo, *J. Am. Chem. Soc.*, 2005, **127**, 7601.
- 15 E. P. Barrett, L. G. Joyner and P. P. Halenda, *J. Am. Chem. Soc.*, 1951, **73**, 373.
- 16 P. I. Ravikovitch and A. V. Neimark, *J. Phys. Chem. B*, 2001, **105**, 6817.
- 17 D. B. Williams and C. B. Carter, *Transmission Electron Microscopy*, Plenum Press, New York, NY, 1996, p. 335.